






Direct and indirect Z-scheme heterostructure-coupled photosystem enabling cooperation of CO₂ reduction and H₂O oxidation

Ying Wang ^{1,2}, Xiaotong Shang¹, Jinni Shen¹, Zizhong Zhang ^{1✉}, Debao Wang², Jinjin Lin¹, Jeffrey C. S. Wu ^{3✉}, Xianzhi Fu¹, Xuxu Wang ^{1✉} & Can Li ^{4✉}

The stoichiometric photocatalytic reaction of CO₂ with H₂O is one of the great challenges in photocatalysis. Here, we construct a Cu₂O-Pt/SiC/IrO_x composite by a controlled photo-deposition and then an artificial photosynthetic system with Nafion membrane as diaphragm separating reduction and oxidation half-reactions. The artificial system exhibits excellent photocatalytic performance for CO₂ reduction to HCOOH and H₂O oxidation to O₂ under visible light irradiation. The yields of HCOOH and O₂ meet almost stoichiometric ratio and are as high as 896.7 and 440.7 μmol g⁻¹ h⁻¹, respectively. The high efficiencies of CO₂ reduction and H₂O oxidation in the artificial system are attributed to both the direct Z-scheme electronic structure of Cu₂O-Pt/SiC/IrO_x and the indirect Z-scheme spatially separated reduction and oxidation units, which greatly prolong lifetime of photogenerated electrons and holes and prevent the backward reaction of products. This work provides an effective and feasible strategy to increase the efficiency of artificial photosynthesis.

¹State Key Laboratory of Photocatalysis on Energy and Environment, Research Institute of Photocatalysis, College of Chemistry, Fuzhou University, 350108 Fuzhou, China. ²Key Lab of Inorganic Synthetic and Applied Chemistry, State Key Lab Base of Eco-Chemical Engineering, College of Chemistry and Molecular Engineering, Qingdao University of Science & Technology, 266042 Qingdao, China. ³Department of Chemical Engineering, National Taiwan University, 10617 Taipei, Taiwan. ⁴State Key Laboratory of Catalysis, Dalian Institute of Chemical Physics, Chinese Academy of Sciences, 116023 Dalian, China. ✉email: z.zhang@fzu.edu.cn; cswu@ntu.edu.tw; xwang@fzu.edu.cn; canli@dicp.ac.cn

Solar-driven photocatalytic conversion of carbon dioxide (CO₂) to valuable organics or solar fuel is an attractive solution to both current energy and environment problems^{1–4}. Reduction of CO₂ under visible light accounting for 45% sunlight energy by water rather than organic compound as an electron donor is the ultimate goal of photocatalysis. Enormous efforts have been devoted to developing a highly efficient photocatalyst for this prospect^{5–7}. However, so far none of photocatalyst systems is satisfactory. Development of novel photocatalyst or system to realize highly efficient conversion of CO₂ remains the focus of future research.

In various reduction products of CO₂, including CO, HCOOH, CH₃OH, HCHO, CH₄, etc., HCOOH is a chemical with wide applications⁸, and even is considered as a promising bio-renewable feedstock for fine chemicals⁹. Although HCOOH as a two-electron-transfer product has the lowest degree of reduction among conversion products of CO₂, all the reported photocatalysts to date still suffer from very low efficiency for HCOOH similar to other organic products^{10–13}. This implies that the photocatalytic reduction of CO₂ to HCOOH is not easier than the reduction to other products. It is well known that the photocatalytic conversion of CO₂ with H₂O involves two half-reactions, i.e. the reduction of CO₂ by the photogenerated electrons and protons, and the oxidation of H₂O by the photogenerated holes. However, most of the reported photocatalysts could not catalyse simultaneously reduction of CO₂ to HCOOH and oxidation of H₂O to O₂¹⁴, and only work in the presence of organic hole-scavengers (e.g. triethanolamine (TEOA), trimethylamine (TEA), or ethylenediaminetetraacetic acid (EDTA))^{15,16}. Such photocatalytic CO₂ reduction at the cost of sacrificial electron donors is not sustainable and likely economically unsound. Even using hole scavenger, the photocatalysts only exhibit a formation rate of HCOOH with tens of micromoles, typically such as some metal-organic framework (MOF) materials (NH₂-MIL-125(Ti), MIL-101(Fe))^{17,18}, inorganic-organic hybrid materials (a binuclear ruthenium(II) complex coupled with Ag/C₃N₄ (ref. 19,20), Cu(I) complex photosensitized Mn(I) complex catalysts²¹), and metal sulfide semiconductors ((Mo–Bi)S_x/CdS)²². The C and Fe co-doped LaCoO₃ was reported to display an HCOOH yield up to 128 μmol g^{−1} h^{−1} without sacrificial reagent, but the oxidation product O₂ was not analysed²³. Such photocatalytic CO₂ reduction without accompanying oxidation half-reaction is inexplicable. The photosynthesis essentially requires the stoichiometric photocatalytic CO₂ reduction and H₂O oxidation which remains a great challenge in photocatalysis²⁴.

Silicon carbide (SiC), a metal-free semiconductor material, possesses a moderate wide band gap (2.4 eV) with an enough negative CB (ca. −1.1 V) to satisfy multielectron reactions of CO₂ reduction with H₂O into carbon fuel and oxygen by solar energy^{25,26}. So it has been considered as a promising photocatalyst for CO₂ conversion since the early research work²⁷. However, the expected photocatalytic efficiency has not been achieved so far. This is due to very large difference between electron and hole migration rates in SiC (electron mobility 700 cm² V^{−1} s^{−1}, hole mobility 90 cm² V^{−1} s^{−1}), which leads to the accumulation of photogenerated holes in the bulk and in turn suppresses the further generation of electrons under light irradiation. This makes the photogenerated carriers to be short-lived, especially the oxidation ability to be poor^{28,29}. Moreover, the pristine SiC is lack of active sites for CO₂ adsorption and activation. Therefore, it is desirable to find the suitable cocatalysts to modify SiC. Additionally, the thermodynamically favourable backward reaction of the produced organics with oxygen on the photocatalyst surface is detrimental to decrease efficiency of CO₂ with pure H₂O in the conversional one-pot reaction. These problems can be concurrently solved by constructing the multi-photocatalyst integration systems in which

the oxidation and reduction reactions are independent in space but coupled in the transfer of photogenerated charges.

Here, we report a Cu₂O–Pt/SiC/IrO_x hybrid photocatalyst, which is prepared by loading the photo-oxidation unit (IrO_x) and the photoreduction unit (Cu₂O–Pt) on SiC surface. This configuration can enhance the lifetime of photogenerated charges and the CO₂ adsorption, and thus the photocatalytic efficiency. Furthermore, we construct a spatially separated reaction system consisting of two reaction chambers analogous to the natural photosynthetic systems. One chamber is loaded with the Cu₂O–Pt/SiC/IrO_x photocatalyst and Fe²⁺ for CO₂ reduction, while the other chamber with the known Pt/WO₃ and Fe³⁺ for H₂O oxidation, and the two chambers are divided by a Nafion membrane that allows Fe²⁺ and Fe³⁺ ions to permeate through. This design facilitates H₂O oxidation half-reaction and suppresses the backward reaction of the products. For the photocatalytic reaction of CO₂ with H₂O to HCOOH and O₂, the system shows very high photocatalytic efficiency under visible light irradiation. The HCOOH yield is as high as 896.7 μmol g^{−1} h^{−1} for the long-term reaction, 527 times higher than that of the pristine SiC (1.7 μmol g^{−1} h^{−1}) in the conversional one-pot reaction. Most importantly, O₂ with a stoichiometric ratio is evolved concurrently. To the best of our knowledge, such high activity for reaction of CO₂ with pure H₂O to HCOOH and O₂ is rarely reported before.

Results and discussion

Configuration and composition of photocatalysts. Figure 1 illustrates the formation process of the photocatalyst Cu₂O–Pt/SiC/IrO_x through the step-by-step photodeposition of Pt, Cu₂O and IrO_x on 3C-SiC (face centre cubic phase of SiC) surface. First, Pt nanoparticles were loaded onto SiC by a simple photodeposition to obtain Pt/SiC sample. Then the resulting Pt/SiC samples were dispersed in aqueous solution containing both Cu²⁺ and IrCl₆^{3−} ions with UV light illumination, which led Cu²⁺ to reduction into Cu₂O species and IrCl₆^{3−} to oxidation into IrO_x. Due to higher work function (5.6 eV) of Pt, the photogenerated electrons on SiC migrated to Pt and the photogenerated holes remained on SiC^{30,31}. Thus the reduction reaction occurred on the Pt particle, while the oxidation reaction did on SiC. We thus concluded that the Cu₂O was deposited on the Pt, while the IrO_x on SiC. The resulting Cu₂O–Pt and IrO_x were located at different region of SiC surface. For comparison, the two reference samples, Cu₂O–Pt/SiC and Pt/SiC/IrO_x, were prepared also in the similar conditions with Cu²⁺-contained solution and IrCl₆^{3−}-contained solution, respectively. The loading amounts of cocatalysts on SiC samples were controlled by the photodeposition time (0.5–15 h) and then were quantified by a quadrupole inductively coupled plasma mass spectrometry (ICP-MS), as summarized in Supplementary Table 1 and Supplementary Note 1. The contents of Pt, Cu₂O and IrO_x on the samples were controlled in the range of 0.83–2.6, 0.52–2.7 and 0.87–3.2 wt%, respectively. Based on the photocatalytic CO₂ reduction results, the optimal amount of Pt, Cu₂O and IrO_x is ascertained to be 1.3%, 1.8% and 2.2 wt% for Cu₂O–Pt/SiC/IrO_x photocatalyst, respectively. For the sake of brevity, hereafter the optimal photocatalyst with 1.3 wt% Pt, 1.8 wt% Cu₂O and 2.2 wt% IrO_x is

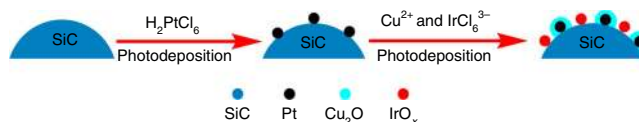


Fig. 1 Formation process of Cu₂O–Pt/SiC/IrO_x by photodeposition.

Schematic representation of Cu₂O–Pt/SiC/IrO_x synthesis via controlled photodeposition.

referred simply to $\text{Cu}_2\text{O-Pt/SiC/IrO}_x$, unless specifically noted otherwise.

The samples were firstly characterized by X-ray powder diffraction (XRD) (Supplementary Fig. 1, Supplementary Note 2). For all samples, except the highly crystalline cubic phase SiC (JCPDS No. 65-0360), no XRD peaks corresponding to the cocatalysts (Pt, Cu_2O and IrO_x) are observed due to their low contents and high dispersion on SiC surface. The BET specific surface area of SiC has a slight reduction from $\sim 18 \text{ m}^2 \text{ g}^{-1}$ for bare SiC to $\sim 14 \text{ m}^2 \text{ g}^{-1}$ for $\text{Cu}_2\text{O-Pt/SiC/IrO}_x$ (Supplementary Fig. 2, Supplementary Note 3), possibly because the cocatalysts with small-size particles block the micropore structure of SiC. The spatial locations of Pt, Cu_2O and IrO_x species on SiC surface were visualized by transmission electron microscopy (TEM) and HRTEM images (Fig. 2). The Pt nanoparticles have a uniform size of ca 2–4 nm and evenly distribute on the surface for all samples, as marked with yellow dotted circle (Fig. 2a, Supplementary Fig. 3). Cu_2O was deposited over Pt nanoparticles to form a $\text{Cu}_2\text{O-Pt}$ intimate contact configuration for both $\text{Cu}_2\text{O-Pt/SiC}$ (Supplementary Fig. 3c, Supplementary Note 4) and $\text{Cu}_2\text{O-Pt/SiC/IrO}_x$ samples (Fig. 2a) as marked with red circle, while the IrO_x species are not deposited at the same location as $\text{Cu}_2\text{O-Pt}$ species for both Pt/SiC/ IrO_x (Supplementary Fig. 3d) and $\text{Cu}_2\text{O-Pt/SiC/IrO}_x$ samples (Fig. 2a), as marked with blue dotted circle. The lattice spacings of $\text{Cu}_2\text{O-Pt/SiC/IrO}_x$ samples (Fig. 2b, Supplementary Fig. 3) are 0.252, 0.226, 0.211 and 0.260 nm assigning to the (111) facet of SiC, (111) facet of Pt, (200) facet of Cu_2O and (101) facet of IrO_2 (refs. 32–35), respectively. The $\text{Cu}_2\text{O-Pt}$ intimate contact structure is further testified by STEM-EDS mapping (Fig. 2c, Supplementary Fig. 4). In the selected area, Pt has the same distribution and appears at almost the same position as Cu, further demonstrating the deposition of Cu_2O over Pt particles. Nevertheless, there is also a part of Cu to be deposited on SiC surface. IrO_x looks like a random deposition on the entire surface of SiC due to very small cluster particles, but it

is separated from $\text{Cu}_2\text{O-Pt}$ on the SiC surface, because the distribution of Ir-L in mapping images (Supplementary Fig. 5, Supplementary Note 4, Fig. 2c) has an obvious difference from that of other elements through careful comparison.

The chemical composition distribution of the outermost layer on SiC surface was further analysed by a high-sensitivity low-energy ion scattering (HS-LEIS) studies. 3 keV $^4\text{He}^+$ HS-LEIS spectra (Fig. 3a) give the signal of the light elements on the outer surface (such as C, O and Si), but have poor sensitivity to Cu, Pt and Ir heavy elements. Figure 3b shows the 5 keV $^{20}\text{Ne}^+$ HS-LEIS spectra of SiC, Pt/SiC, $\text{Cu}_2\text{O-Pt/SiC}$, Pt/SiC/ IrO_x and $\text{Cu}_2\text{O-Pt/SiC/IrO}_x$. Pt element is detected on the outmost surface for Pt/SiC. Only Cu element is observed on $\text{Cu}_2\text{O-Pt/SiC}$, clearly indicating that Cu_2O is deposited on the surface of Pt nanoparticles. Although HS-LEIS peaks of Pt and Ir cannot be resolved using 5 keV $^{20}\text{Ne}^+$ because their atomic mass is too close, it should be noted that intensity of the fused peaks of Pt and Ir at 3367 eV for Pt/SiC/ IrO_x is significantly stronger than that of sole Pt peak in Pt/SiC. This indicates that both IrO_x and Pt coexist on the outermost surface of Pt/SiC/ IrO_x . However, the peak at 3367 eV for $\text{Cu}_2\text{O-Pt/SiC/IrO}_x$ samples weakens significantly as compared with Pt/SiC/ IrO_x . Since Pt is covered by Cu_2O in $\text{Cu}_2\text{O-Pt/SiC/IrO}_x$, the low peak at 3367 eV of $\text{Cu}_2\text{O-Pt/SiC/IrO}_x$ can be only assigned to IrO_x on the outermost surface. Therefore, the HS-LEIS results constitute another strong evidence that the $\text{Cu}_2\text{O-Pt}$ and IrO_x cocatalysts are spatially separated on SiC surface for $\text{Cu}_2\text{O-Pt/SiC/IrO}_x$.

The chemical states of the Pt, Cu and Ir elements in samples were analysed by XPS (Fig. 4). Three sets of Pt 4f XPS peaks can be assigned to metallic Pt^0 and partially oxidized Pt^{2+} and Pt^{4+} species³⁶. The ratio of Pt^0 is calculated to be accounting for $70 \pm 4\%$ of the sum Pt species for the all Pt-contained samples (Supplementary Table 2). Cu species and Ir species are mainly in the state of Cu_2O and mixed valence oxides (IrO_x), respectively^{37,38}. Nevertheless, the binding energies (BE) of Pt, Cu or Ir have obvious differences among samples. For Pt/SiC, the BE of Pt 4f_{7/2} and Pt 4f_{5/2} are respectively 70.8 and 74.1 eV, which are lower than that of the pure metallic Pt (Pt 4f_{7/2} = 71.2 eV)³⁹. This is because the electron transfer occurs from the SiC substrate to Pt particles with higher work function^{40,41}. When Cu_2O is subsequently deposited on Pt/SiC to form $\text{Cu}_2\text{O-Pt/SiC}$, the BE of Pt 4f_{7/2} shifts towards higher energy (71.1 eV), but is still slight lower than that of metallic Pt, indicating the electron transfer still from SiC to Cu_2O under mediation of Pt nanoparticles. On the contrary, when IrO_x is deposited onto Pt/SiC to form Pt/SiC/ IrO_x , the BE of Pt 4f shifts to lower position. This indicates that IrO_x deposition induces the electron transfer from IrO_x to the SiC surface and thus enhances the electron transfer to Pt particles. In the case of the co-deposition of IrO_x and Cu_2O on Pt/SiC, the BE of Pt 4f in $\text{Cu}_2\text{O-Pt/SiC/IrO}_x$ is comparable with $\text{Cu}_2\text{O-Pt/SiC}$. This demonstrates that the electrons are finally transferred from both SiC and IrO_x into Cu_2O . As a result, the BE of Cu 2p for $\text{Cu}_2\text{O-Pt/SiC/IrO}_x$ is also lower than that of $\text{Cu}_2\text{O-Pt/SiC}$. In reverse, the BE of Ir 4f for $\text{Cu}_2\text{O-Pt/SiC/IrO}_x$ is slightly positively shifted as compared with Pt/SiC/ IrO_x . The above results show the existence of the strong interfacial interaction between co-catalyst and SiC, which would be favourable for the electron migration and transfer in $\text{Cu}_2\text{O-Pt/SiC/IrO}_x$.

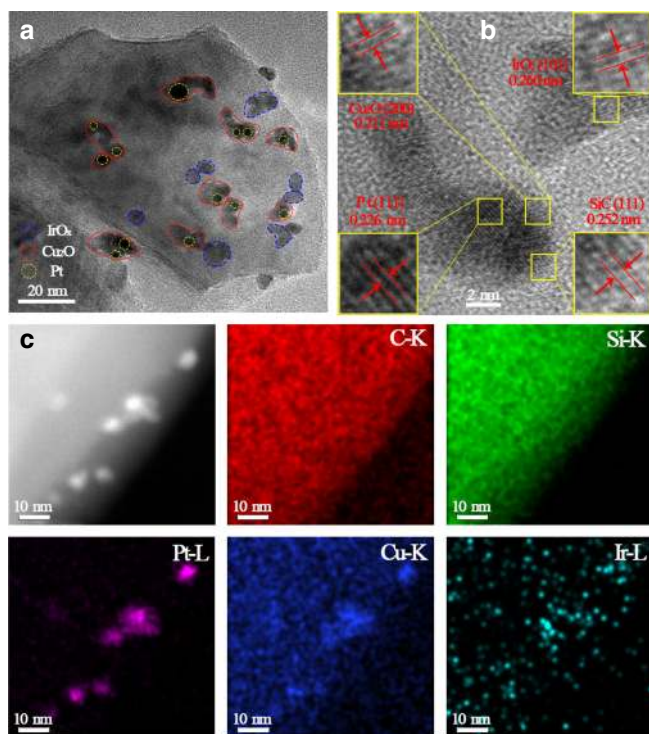


Fig. 2 Spatial location of cocatalysts. **a** TEM, **b** HRTEM images and **c** STEM image and corresponding EDS mapping profiles for C-K, Si-K, Pt-L, Cu-K and Ir-L of $\text{Cu}_2\text{O-Pt/SiC/IrO}_x$.

Photocatalytic performance of CO_2 reduction with H_2O . The photocatalytic CO_2 reduction was performed in the spatially separated reaction system. Fe^{2+} and Fe^{3+} were added respectively in the CO_2 -reduction compartment and the H_2O -oxidation compartment in the beginning of the reaction (see Supplementary Fig. 6)^{42,43}. During the photoreaction process, Fe^{3+} and Fe^{2+}

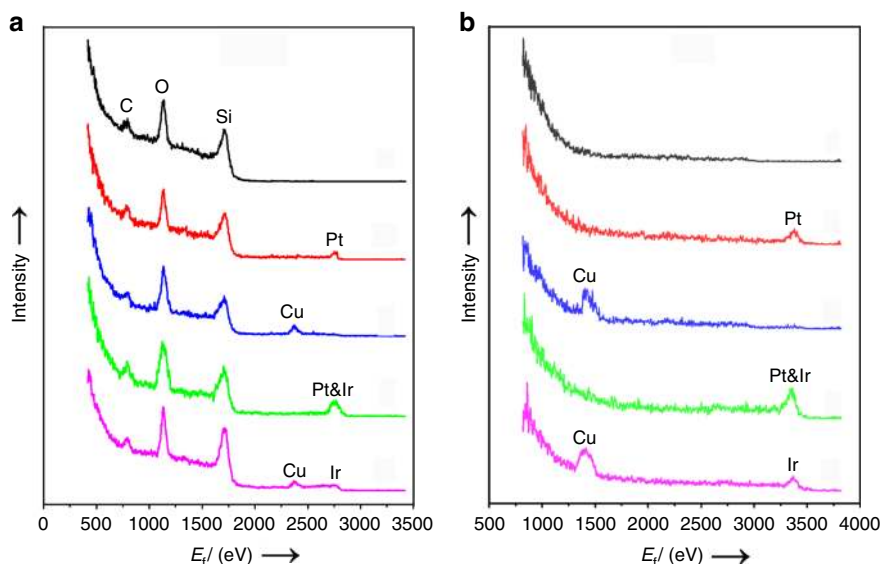


Fig. 3 The chemical composition on the outermost surface. HS-LEIS spectra using **a** 3 keV $^4\text{He}^+$ and **b** 5 keV $^{20}\text{Ne}^+$ for the samples: SiC (black), Pt/SiC (red), Cu_2O -Pt/SiC (blue), Pt/SiC/ IrO_x (green) and Cu_2O -Pt/SiC/ IrO_x (pink).

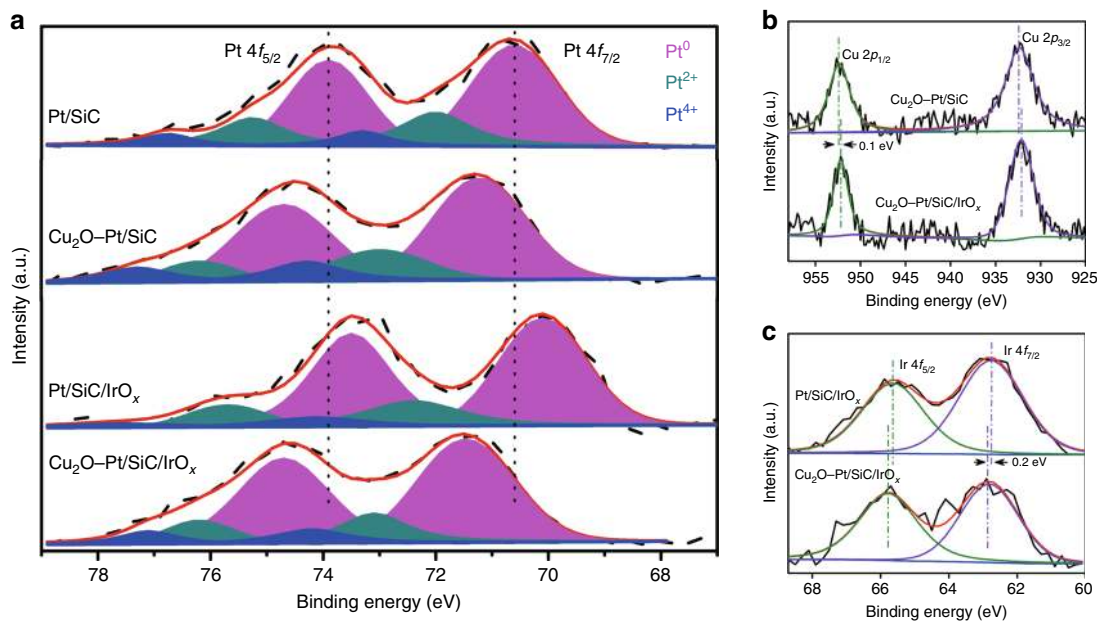


Fig. 4 The chemical states of cocatalysts. **a** Pt 4f XPS spectra, **b** Cu 2p XPS spectra, and **c** Ir 4f XPS spectra of Pt/SiC, Cu_2O -Pt/SiC, Pt/SiC/ IrO_x and Cu_2O -Pt/SiC/ IrO_x samples.

ions are able to permeate through the Nafion membrane driven by the concentration gradient. The photocatalytic activities of the samples for the reaction of CO_2 with H_2O were tested under visible light irradiation in order to find out the optimal contents of cocatalysts, as shown in Fig. 5 and Supplementary Table 1. HCOOH is detected as a main product for all photocatalysts. The bare SiC only shows $24.1 \mu\text{mol g}^{-1} \text{h}^{-1}$ of HCOOH yield. Over Pt/SiC samples, the HCOOH yield shows a volcanic curve with increasing Pt contents and the highest HCOOH yield ($57.7 \mu\text{mol g}^{-1} \text{h}^{-1}$) occurs at 1.3 wt% Pt content (Fig. 5a). On the Cu_2O -Pt/SiC sample with 1.3 wt% Pt, the product HCOOH shows the highest yield ($304.6 \mu\text{mol g}^{-1} \text{h}^{-1}$) at 1.8 wt% content of Cu_2O (Fig. 5b). On the Pt/SiC/ IrO_x with the optimum Pt content (1.3 wt%), the optimal loading content of IrO_x is 2.2 wt% at which the HCOOH yield is ca. $472.0 \mu\text{mol g}^{-1} \text{h}^{-1}$ (Fig. 5c). When both IrO_x and Cu_2O are simultaneously

deposited on the optimal Pt/SiC, the highest yield of HCOOH, $896.7 \mu\text{mol g}^{-1} \text{h}^{-1}$, occurs at ca. 2.2 wt% of IrO_x and 1.8 wt% of Cu_2O . When Cu_2O content is higher than 1.8 wt%, further increasing Cu_2O photodeposition induces more amount of Cu_2O on both Pt particles and the exposed SiC surface. The deposited Cu_2O on SiC could block the optical absorption of SiC, and an over-thick Cu_2O layer on Pt surface is also unfavourable to CO_2 reduction on Cu_2O -Pt³². The higher IrO_x contents <2.2 wt%, the more active sites of IrO_x are provided to enhance the Fe^{2+} oxidation. However, an excess amount of IrO_x may lead to the growth of IrO_x into large particles on SiC surface, which is harmful to the photocatalytic reaction. The HCOOH yield over the optimal Cu_2O -Pt/SiC/ IrO_x is almost 37 times of the activity of the bare SiC. To the best of our knowledge, the photocatalytic efficiency of our system is substantially higher than that of other various photocatalysts

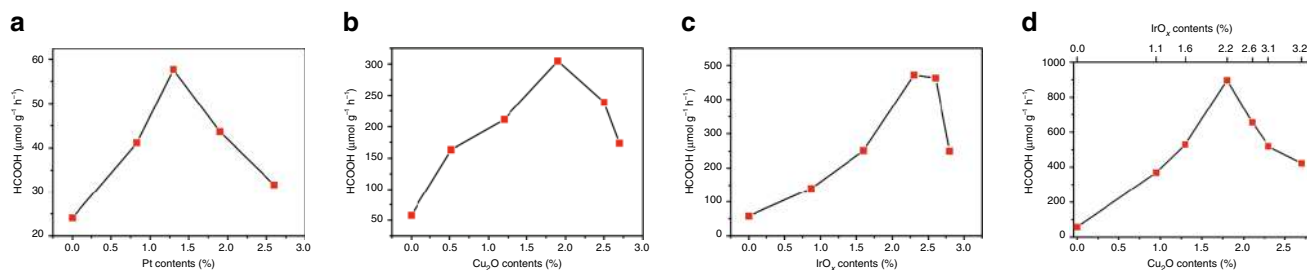


Fig. 5 The optimal contents of cocatalysts for CO₂ reduction. Change in HCOOH evolution rate **a** on Pt/SiC with increasing Pt content, **b** on Cu₂O–Pt (1.3 wt%)/SiC with increasing Cu₂O, **c** on Pt (1.3 wt%)/SiC/IrO_x with increasing IrO_x, and **d** on Cu₂O–Pt/SiC/IrO_x with increasing Cu₂O and IrO_x, in spatially separated reactor under visible light irradiation. Reaction conditions: 50 mg SiC-based photocatalyst and 300 mL of 2 mM FeCl₂ aqueous solution were placed in the CO₂-reduction chamber, 100 mg Pt/WO₃ and 300 mL of 2 mM FeCl₃ aqueous solution in the H₂O oxidation chamber, the pH of solution was adjusted to 2.3 by adding hydrochloric acid to prevent precipitation of the iron ions aqueous solution.

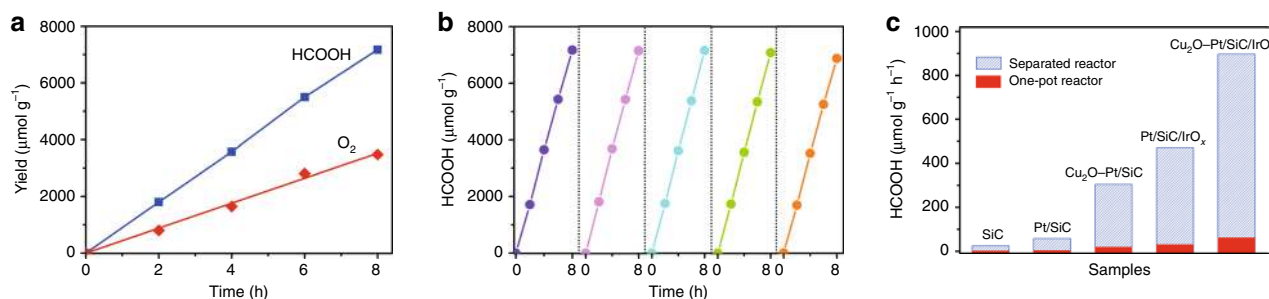


Fig. 6 Photocatalytic performance of CO₂ reduction with H₂O. **a** Evolutions of HCOOH and O₂ as a function of illumination time and **b** cycle experiment of HCOOH evolution in the spatially separated reaction system with Cu₂O–Pt/SiC/IrO_x as the reduction side photocatalyst. **c** Comparison for the HCOOH evolution between in the spatially separated reaction system and in the conventional one-pot reactor with different samples as the reduction side photocatalyst.

reported so far (seen activity comparison in Supplementary Table 3).

O₂ is confirmed as main product evolving in the Pt/WO₃ oxidation chamber of the separated reaction system. Figure 6a shows the production of O₂ in the Pt/WO₃ chamber and HCOOH in the Cu₂O–Pt/SiC/IrO_x chamber vs. irradiation time. Both yields of HCOOH and O₂ increase linearly, and reach 7200 and 3300 μmol g⁻¹ during 8 h photocatalytic reactions, respectively. Moreover, the ratio of product O₂ to HCOOH is close to the stoichiometric number of reaction (2CO₂ + 2H₂O → 2HCOOH + O₂) in the whole process. Influence of the Pt amount of Pt/WO₃ on the photocatalytic O₂ and HCOOH evolutions in the separated reaction system was also investigated (Supplementary Fig. 7). As decreasing Pt content to 0.5 wt% of Pt/WO₃, the O₂ and HCOOH yields decrease to 296.6 and 618.7 μmol g⁻¹ h⁻¹, respectively. However, the ratio of O₂ to HCOOH is still close to the stoichiometric number. When the Pt content increases to 1.5 wt%, both O₂ and HCOOH evolution is almost the same as that of 1.0 wt% Pt. The 1.0 wt% Pt content is optimal for the Pt/WO₃ in the separated reaction system. Obviously, Pt content of Pt/WO₃ does not affect the stoichiometric ratio of product HCOOH to O₂. This is because Fe³⁺/Fe²⁺ redox couple acts as the electron transfer medium between CO₂ reduction and H₂O oxidation by the concentration diffusion through the Nafion membrane, which makes the reaction stoichiometrically proceeded in the reaction process. However, the HCOOH yield shows a downtrend as prolonging the reaction time (Supplementary Fig. 8). The decrease of activity is because pH value of the reaction solution is increased from 2.3 at the initial stage to 4.5 after 12 h reaction along with the consumption of H⁺ in the process of CO₂ reduction. The increase in solution alkalinity can result in hydrolysis of Fe³⁺ to FeOOH or Fe(OH)₃, as confirmed by the Fe 2p XPS spectrum of the sample after the reaction

(Supplementary Fig. 9). However, the activity is highly stable in five cycles of total 40 h (Fig. 6b) when the Cu₂O–Pt/SiC/IrO_x is centrifuged out and then added to the fresh solution before each new cycle. Therefore, the increase in solution alkalinity during the photocatalytic reaction is one of reasons effecting stability of the reaction, which should be avoided by increasing solution acidity.

The Cu₂O–Pt/SiC/IrO_x samples before and after the photocatalytic reaction were characterized by XPS (Supplementary Fig. 10), indicating some differences in chemical states of Pt, Ir and Cu. However, the changes of metal states are likely to have no significantly influence or be not main factor on the photocatalytic activity stability. (i) For Pt, the XPS Pt 4f peaks narrow down and the shoulder peaks become weak for the used sample, but the BE values of main peaks keep almost unchanged before and after the photocatalytic reaction. The main peaks at the BEs of 74.7 eV (Pt 4f 5/2) and 71.5 eV (Pt 4f 7/2) are attributed to Pt(0). The shoulder peaks are belonged to Pt²⁺ and Pt⁴⁺ species. It can be seen that a part of high valence Pt species were translated also into Pt (0) after longtime reaction, which could be beneficial to the photocatalysis. (ii) For IrO_x, the Ir 4f peaks not only become narrow but also shift towards lower energy after the photocatalytic reaction. The wide Ir 4f peaks of both the fresh and the used samples cover Ir⁰, Ir³⁺ and Ir⁴⁺ species, indicating the mix valence state feature of IrO_x. Accordingly, the Ir 4f_{7/2} peak can be deconvoluted into a contribution of Ir⁰ (61.3 eV), Ir⁴⁺ (62.4 eV) and Ir³⁺ (63.5 eV) species^{44–46}. The phenomena are universal for Ir-loaded catalysts, which is also the reason why iridium oxide is usually be expressed as IrO_x rather than IrO₂⁴⁷. It is estimated from the peak intensities that the contents of Ir⁴⁺ are increased, while Ir³⁺ contents are decreased in the used sample as compared with the fresh sample (see Supplementary Table 4). Such a change in the Ir 4f XPS spectra can be explained by the changes in the crystallinity and coordination numbers^{48,49}. For the fresh sample,

the broader and higher BE peaks suggest the existence of partial amorphous or high oxygen coordinated Ir species. For the used sample, the shift of BE of Ir 4f peak towards lower energy indicates an increase in the rutile phase IrO₂ during the photocatalytic process since the IrO_x could be mainly excited from the d(t_{2g}) to the d(e_g) band (1.5–2.75 eV) under visible light irradiation based on the literature⁵⁰. It is possible that the change in Ir valence state or crystallinity do not affect the photoinduced d–d transition and thus photocatalytic performance. (iii) As for Cu₂O, the Cu 2p XPS spectrum shows a minor change. The BEs of the main peaks of Cu 2p remain almost the same before and after the reaction, only a minuscule shift towards lower energy. We could not exclude the possibility that a small amount of Cu(I) was translated into Cu(0) after the photocatalytic reaction. Because some Cu₂O is deposited synchronously on the SiC surface, the small change of Cu valence state can occur partly for these Cu₂O species, which could have no remarkable influence on the photocatalytic performance.

Other two control experiments were carried out also. When ¹³CO₂ instead of CO₂ was used as a reactant, ¹³C NMR analysis for the reaction solution verifies that only a strong peak at 171.5 ppm attributed to the ¹³C in H¹³COOH was observed (Supplementary Fig. 11)⁵¹. When CO₂ was not added in the reaction system, no HCOOH was detected. These results show that the product HCOOH is formed from the photocatalytic CO₂ reduction. As H₂¹⁸O instead of H₂O is used as the reactant in a small dose simulated reaction, the mass spectroscopy analysis gives a main peak at *m/z* = 36 corresponding to ¹⁸O₂ (Supplementary Fig. 12), confirming the product O₂ originating from H₂O oxidation. Careful analysis reveals that except HCOOH no carbon-containing products, such as CO, HCHO and CH₄, come into being in the gas phase. Nevertheless, there is only a very slight amount of H₂ to evolve as a by-product (Supplementary Fig. 13), implying existence of competition between the reduction of H⁺ to H₂ and the reduction of CO₂ to HCOOH by photogenerated electrons. In the absence of CO₂ atmosphere, however, only a slightly enhanced amount of H₂ evolves in the gas phase (Supplementary Fig. 14), although the photocatalytic reaction is performed in the acidic aqueous solution. This indicates that the SiC-based photocatalyst is not good for H₂ evolution from water, which may be because that it lacks the active sites or has high overpotential for the H₂ evolution. However, for the reduction of CO₂, the SiC-based photocatalyst can be particularly effective.

The photocatalytic activity for the reaction of CO₂ with H₂O was also evaluated in the conventional one-pot reactor, where we added simultaneously SiC-based catalyst, Pt/WO₃ and Fe²⁺/Fe³⁺. HCOOH and O₂ are also detected as main products. Figure 6c compares the HCOOH yields under two different reaction modes (see also Supplementary Table 5). It can be seen that all the samples show much higher HCOOH yield with the spatially separated reaction system than with the one-pot reaction mode. For SiC, Pt/SiC, Cu₂O–Pt/SiC, Pt/SiC/IrO_x and Cu₂O–Pt/SiC/IrO_x photocatalyst, the HCOOH yield is 1.7, 3.5, 18.6, 30.4 and 61.5 μmol g⁻¹ h⁻¹ with the one-pot reaction, while it is 24.1, 57.7, 304.6, 472.0 and 896.6 μmol g⁻¹ h⁻¹ with the spatially separated system, respectively. Obviously, the photocatalytic activity of the spatially separated system is ca ~15 times higher than that in the one-pot reaction reactor for each photocatalyst. In the one-pot reaction system, the backward reaction of HCOOH re-oxidization by O₂ should be one of the reasons for the low evolution of HCOOH and O₂. Both Fe³⁺ competing with CO₂ for the generated electrons and Fe²⁺ competing with H₂O for the photogenerated holes could also take place at the same time. However, the effects of the later could be weaker than that of the

former, because the evolutions of HCOOH and O₂ are lower if no adding Fe³⁺ and Fe²⁺ (see the first column in Supplementary Table 5). This could be one of reasons for high efficiency of the spatially separated system. However, the reasonableness of this inference requires the following two premises: the product HCOOH (i) does not diffuse to the oxygen evolution chamber from the reduction chamber through the Nafion membrane and (ii) is not oxidized in the reduction chamber by the Fe³⁺, with increase in the production of HCOOH. Accordingly, two additional experiments were done. The permeation of HCOOH across the Nafion membrane from the HCOOH solution (1200 μmol L⁻¹, corresponding to the maximum yield of HCOOH in the separated system for 8 h reaction) to pure H₂O is determined firstly. Only very limited amount of HCOOH (<5%) is diffused to the pure water across the Nafion membrane within 8 h (Supplementary Fig. 15). Another experiment is the solution (pH = 2.3) with HCOOH (1200 μmol L⁻¹) and Fe²⁺/Fe³⁺ (2 mmol L⁻¹) under visible light illumination. The concentration of HCOOH remains almost unchanged (Supplementary Fig. 16). These indicate that our new system is indeed effective to prevent the backward reaction. The wavelength-dependent evolution of HCOOH was also performed to gain the apparent quantum yield (AQY) (Supplementary Fig. 17). Obviously, the AQY of HCOOH evolution on the optimal Cu₂O–Pt/SiC/IrO_x sample is well matched with the optical absorption spectra. Under 400 nm light irradiation, the AQY of HCOOH evolution can be reached near 1.44%.

The in situ CO₂ adsorption FT-IR spectra. The photocatalytic activity of Cu₂O–Pt/SiC/IrO_x is always higher than that of the other samples both in the spatially separated system and in the one-pot reactor. The HCOOH yield on the optimal Cu₂O–Pt/SiC/IrO_x sample in the spatially separated system is 37 and 527 times higher than that on the bare SiC in the spatially separated system and in the one-pot reactor, respectively. Obviously, the high efficiency of Cu₂O–Pt/SiC/IrO_x for the reaction of CO₂ with H₂O to HCOOH can be related to the photocatalyst surface feature. The in situ CO₂ adsorption FT-IR spectra were measured to gain insight into the effect of surface feature. As shown in Fig. 7a, all photocatalysts show the multiple IR adsorption peaks of CO₂ in the range of 2200–2500 cm⁻¹ in the dark. It is noteworthy that both the samples containing Cu, i.e. Cu₂O–Pt/SiC and Cu₂O–Pt/SiC/IrO_x, show much stronger CO₂ adsorption band than nude SiC, Pt/SiC and Pt/SiC/IrO_x. This implies that CO₂ molecules are mainly adsorbed on the Cu₂O co-catalyst in Cu₂O–Pt/SiC and Cu₂O–Pt/SiC/IrO_x^{32,52}. Figure 7b shows the in situ CO₂ adsorption FT-IR spectra on Cu₂O–Pt/SiC/IrO_x in the range of 1700–1200 cm⁻¹ after and before light irradiation, which is a reflection of chemical adsorption. No absorption attributable to O₂ species appears on Cu₂O–Pt/SiC/IrO_x in the absence of CO₂ gas (omitted). As introduction of CO₂, Cu₂O–Pt/SiC/IrO_x shows very weak several absorption peaks before visible light irradiation. However, three strong absorption bands appear upon visible light irradiation. Both the wide absorption band at 1394 cm⁻¹ and the weak band at 1503 cm⁻¹ are ascribed to bidentate carbonate species bonded to the Cu₂O surface, while the absorption band at 1262 cm⁻¹ is assigned to a monodentate carbonate to the Cu₂O surface^{53,54}. This demonstrates that CO₂ molecules are activated at room temperature by the Cu₂O co-catalyst on Cu₂O–Pt/SiC/IrO_x surface under light irradiation. Moreover, the acidic aqueous solution (pH = 2.3) is helpful for formation of the carboxyl radical intermediate (·COOH) or the formate anion (HCOO⁻) that is further easily converted into HCOOH^{14,55}. This could be the second possible reason for the high efficiency of the spatially separated system. High selectivity of product HCOOH may be related to the different reaction mechanism dependent on the

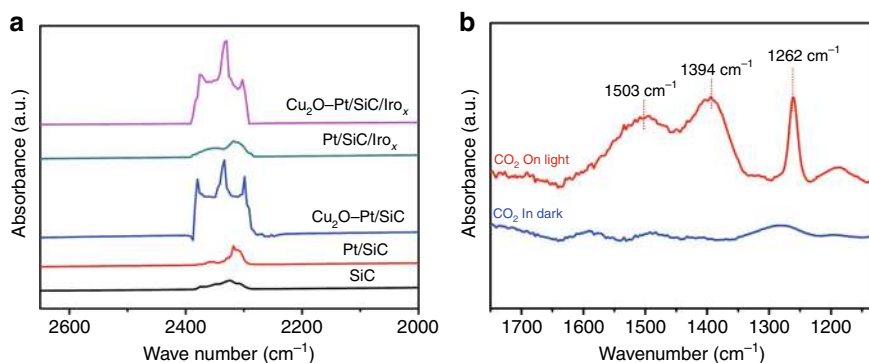


Fig. 7 Adsorption of CO₂ on photocatalysts. a In situ FT-IR spectra of CO₂ adsorbed on different photocatalysts. **b** In situ FT-IR spectra of CO₂ adsorbed on Cu₂O-Pt/SiC/IrO_x before and after visible light irradiation. All the spectra are the difference spectra between after and before CO₂ adsorption.

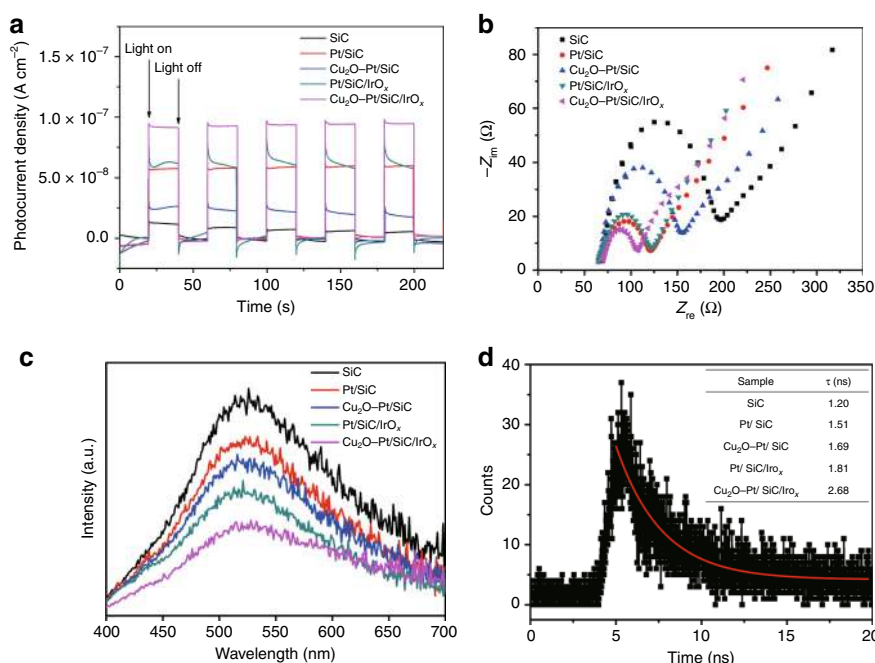


Fig. 8 Separation efficiency and lifetime of carriers. a Periodic on/off photocurrent response, **b** AC Impedance and **c** PL (photoluminescence) spectra for different photocatalysts. **d** Time-resolved photoluminescence spectroscopy of Cu₂O-Pt/SiC/IrO_x.

reaction conditions, such as the photocatalyst states (defects, crystal faces, doping, etc.), reaction conditions (temperature, pH, CO₂ concentration, reactant phase, etc.), co-catalyst and so on. In the gas (CO₂, H₂O vapour)–solid (catalyst) mode, it has been found that the SiC-based composite (MoS₂/SiC) photocatalyzed the CO₂ reduction into CH₄ undergoing HCOOH, HCHO and CH₃OH intermediates on SiC surface by the hydrogenation pathways²⁶. In the present work, the reaction is conducted in gas (CO₂)–liquid (H₂O)–solid(catalyst) mode and the acidic aqueous solution. In addition, the reduction of CO₂ occurs on the Cu₂O sites rather than SiC, which is helpful for formation of the carboxyl (hydroxyformyl) radical intermediate ·COOH and HCOOH^{14,56}.

Photoelectrochemical properties of Cu₂O-Pt/SiC/IrO_x. The photoelectrochemical responses and the photoluminescence spectra of these photocatalysts were measured. Figure 8a, b shows the photocurrents and AC impedance of the different samples. The photocurrents increase in order of SiC, Cu₂O-Pt/SiC, Pt/SiC, Pt/SiC/IrO_x and Cu₂O-Pt/SiC/IrO_x, and the AC impedance values decrease in the same order. Obviously, Cu₂O-Pt/SiC/IrO_x

shows the biggest photocurrent and the smallest AC impedance, indicating the highest electron transfer rate and separation efficiency. However, the sample Cu₂O-Pt/SiC and Pt/SiC show a slight abnormality, i.e. both the photocurrent increase order and the AC impedance decrease order are inconsistent with the increase order of photocatalytic activity. This can be explained by the dependence of photocatalytic activity on not only the transfer rate and separation efficiency of photogenerated charges but also the surface chemistry characteristics of photocatalyst. Figure 8c is the steady-state photoluminescence (PL) spectra of these samples. The PL intensities decrease in accordance with the order of SiC, Pt/SiC, Cu₂O-Pt/SiC, Pt/SiC/IrO_x and Cu₂O-Pt/SiC/IrO_x, which agree with the change in the photocatalytic activity. Since low PL intensity corresponds to low recombination rate of photogenerated charges, the lowest PL intensity indicates the smallest recombination rate of photogenerated charge for Cu₂O-Pt/SiC/IrO_x. Figure 8d shows the time-resolved photoluminescence spectroscopy of these samples (see detailed Supplementary Fig. 18), and the corresponding average lifetimes (τ) of charge carriers (the inset table). The τ value of nude SiC is about 1.2 ns, consistent with the reported literature⁵⁷. Loading Pt, Cu₂O and

IrO_x nanoparticles lead to an increase in the lifetime τ . In these samples, $\text{Cu}_2\text{O-Pt/SiC/IrO}_x$ has the highest τ value. The increase in the lifetime τ of the charge carriers could increase the probability of their involvement in photocatalytic reactions before recombination^{58–60}. So, increases in the transfer rate, separation efficiency and lifetime of photogenerated charges could be the third reason for high efficiency of the spatially separated system.

Photocatalytic mechanism of the spatially separated system.

The next issue is the electron structure of $\text{Cu}_2\text{O-Pt/SiC/IrO}_x$ and the photocatalytic mechanism of the spatially separated system. The electron structure parameters of SiC and Cu_2O were reckoned by combination of the UV-Vis diffuse reflection spectra with the Mott-Schottky analysis (Supplementary Fig. 19). The optical absorption edge of the nude SiC is at 501 nm. The band gap energy and the conduction band (CB) potential of SiC are ca. 2.48 eV and -1.08 V (vs. SHE), respectively. The parent Cu_2O is estimated to have a band gap of 1.98 eV and CB of -1.28 V. It has been reported that the IrO_x could be excited from the $d(t_{2g})$ to the $d(e_g)$ band (1.5–2.75 eV) by visible irradiation and from the O-p band to the $d(e_g)$ (>3.0 eV) band by ultraviolet irradiation, and its CB is $+0.35$ V⁵⁰. For the $\text{Cu}_2\text{O-Pt/SiC/IrO}_x$ photocatalyst, $\text{Cu}_2\text{O-Pt}$ and IrO_x cocatalysts are separated each other on SiC surface, and Pt is sandwiched between Cu_2O and SiC. Thus, $\text{Cu}_2\text{O-Pt/SiC/IrO}_x$ is suggested to have the energy band alignment in Fig. 9a.

If the Cu_2O co-catalyst directly contacts with SiC without Pt, the photoelectron transfers on the resulting $\text{Cu}_2\text{O/SiC}$ composite is speculated to follow the Z-scheme transfer from SiC to Cu_2O , which has been reported in many literatures^{61–63}. Such Z-scheme photoelectron transfer was verified by a photocatalytic probe reaction. When the water solution containing the $\text{Cu}_2\text{O/SiC}$ sample and H_2PtCl_6 was illuminated by UV light, the reduction reaction ($\text{PtCl}_6^{2-} + 4e^- \rightarrow \text{Pt} + 6\text{Cl}^-$) would occur on the $\text{Cu}_2\text{O/SiC}$ surface. The TEM image clearly indicates preponderant photodeposition of Pt particles over Cu_2O particle rather than over SiC surface (Supplementary Fig. 20), unambiguously verifying the Z-scheme electron transfer, i.e. the transfer of photogenerated electron from the CB of SiC to the VB of Cu_2O . For our $\text{Cu}_2\text{O-Pt/SiC/IrO}_x$ sample, we can reasonably conclude that the Z-scheme electron transfers from the CB of SiC to the valence band (VB) of Cu_2O would be accelerated by the Pt nanoparticles located between Cu_2O and SiC, due to the excellent conductivity and high work function of Pt. The controlled experiment shows that the $\text{Cu}_2\text{O/SiC}$ displays the HCOOH evolution of about $40.5 \mu\text{mol g}^{-1} \text{h}^{-1}$, which is little higher than that of the pristine SiC but much lower than that of $\text{Cu}_2\text{O-Pt/SiC}$

samples (Supplementary Fig. 21). This means that contribution of the Cu_2O deposited on SiC surface to the activity is very small, and the high activity is mainly due to the embedding of Pt in the interface between Cu_2O and SiC. The photocatalytic CO_2 reduction performances of $\text{Cu}_2\text{O/SiC/IrO}_x$ and $\text{Pt-Cu}_2\text{O/SiC/IrO}_x$ were also compared with that of $\text{Cu}_2\text{O-Pt/SiC/IrO}_x$ (Supplementary Fig. 21). Much lower activities of $\text{Cu}_2\text{O/SiC/IrO}_x$ and $\text{Pt-Cu}_2\text{O/SiC/IrO}_x$ than that of $\text{Cu}_2\text{O-Pt/SiC/IrO}_x$ indicates likewise that the Pt sandwiched between the interface of Cu_2O and SiC is more beneficial to the transfer of photogenerated electrons from SiC to Cu_2O thus enhances CO_2 reduction. Simultaneously, another direct Z-scheme photoelectron transfer occurs at the interface between IrO_x and SiC, because SiC has much more positive VB than CB of IrO_x . As a result, SiC, Cu_2O and IrO_x in $\text{Cu}_2\text{O-Pt/SiC/IrO}_x$ all are excited by visible light, the photogenerated electrons from the CB of IrO_x ($+0.35$ V) would transfer towards the VB of SiC ($+1.40$ V). Synchronously, the photogenerated electrons from the CB of SiC (-1.08 V) would transfer towards Pt nanoparticles, and then towards the VB of Cu_2O ($+0.70$ V) where they combine with the photogenerated holes at Cu_2O . On the whole, the coupled direct Z-scheme processes result in the photogenerated electrons accumulating in the CB of Cu_2O (-1.28 V) where the adsorbed CO_2 is reduced into HCOOH [$E(\text{CO}_2/\text{HCOOH}) = -0.61$ V], while the photogenerated holes on the VB of IrO_x ($t_{2g} = +1.85$ V) to oxidize Fe^{2+} into Fe^{3+} [$E(\text{Fe}^{2+}/\text{Fe}^{3+}) = +0.77$ V]^{64,65}. Meanwhile, in the H_2O oxidation chamber, Pt/WO_3 is excited also by visible irradiation. The photogenerated electrons would transfer from the CB of WO_3 ($+0.74$ V) towards Pt and then reduce Fe^{3+} into Fe^{2+} [$E(\text{Fe}^{2+}/\text{Fe}^{3+}) = +0.77$ V], while the photogenerated holes of WO_3 ($+2.06$ V) would oxidize H_2O to O_2 ($E = +1.23$ V). As shown in Fig. 9b, the overall photocatalytic system follows indirect Z-scheme mechanism similar to the natural photosynthesis, i.e. the photocatalytic CO_2 reduction half-reaction and the photocatalytic H_2O oxidation half-reaction take place at two separated reactors by the relaying role of $\text{Fe}^{3+}/\text{Fe}^{2+}$ redox couple. To prove that the total reaction is a combination of the spatially separated reduction and oxidation, two controlled experiments were done. When the water solution containing photocatalyst Pt/WO_3 and Fe^{3+} is illuminated with visible light, O_2 is generated also as a main product (Supplementary Fig. 22a), validating the oxidation half-reaction in the left side of Fig. 9b. When the solution containing H_2O , $\text{Cu}_2\text{O-Pt/SiC/IrO}_x$, Fe^{2+} and CO_2 is illuminated with visible light, HCOOH is detected also as main product (Supplementary Fig. 22b), validating the reduction half-reaction in the right side of Fig. 9b. Therefore, $\text{Fe}^{3+}/\text{Fe}^{2+}$ redox couple makes the reduction of CO_2 to HCOOH on

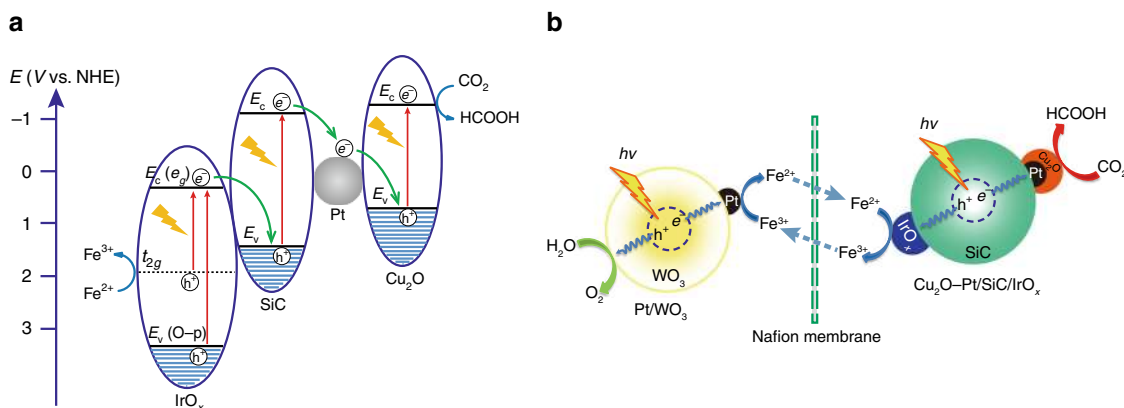


Fig. 9 Electronic structure and photocatalytic mechanism. **a** The electron transfer processes in $\text{Cu}_2\text{O-Pt/SiC/IrO}_x$ under light illumination. **b** The proposed mechanism of the separated system for the efficient CO_2 reduction and O_2 evolution.

$\text{Cu}_2\text{O-Pt/SiC/IrO}_x$ and the oxidation of H_2O to O_2 on Pt/WO_3 integrated into the one system like the natural photosynthetic systems. It must be mentioned that the usage mode of Fe^{3+} and Fe^{2+} has little impact on the reaction efficiency. When the $\text{Fe}^{2+}/\text{Fe}^{3+}$ mixed solution was used in both cells of the separated reaction system, HCOOH was produced steadily with the reaction time (Supplementary Fig. 23), and its generation rate is $629.8 \mu\text{mol g}^{-1} \text{h}^{-1}$. When Fe^{2+} and Fe^{3+} were separately loaded in the CO_2 -reduction compartment and the H_2O -oxidation compartment, the initial generation rate of HCOOH is $896.6 \mu\text{mol g}^{-1} \text{h}^{-1}$. Obviously, the separate addition of Fe^{2+} solution and Fe^{3+} solution in both compartments is more efficient than the loading of $\text{Fe}^{2+}/\text{Fe}^{3+}$ mixed solution in both compartments for the photocatalytic reaction in the separated reaction system. But the separated use mode of Fe^{2+} and Fe^{3+} can only improve initiate photoreaction efficiency. When the redox reaction reaches dynamic steady state, the concentrations of Fe^{2+} and Fe^{3+} also reach a constant gradient in both sides to maintain counter diffusion. Fe^{2+} and Fe^{3+} are not evenly dispersed in either cell according to previous study due to osmosis of Fe ions through Nafion membrane⁶⁶. Even though the concentration of Fe^{2+} and Fe^{3+} is equal in the reaction compartments, the H_2O oxidation and CO_2 reduction can proceed over the photocatalysts due to the different adsorption property of $\text{Fe}^{2+}/\text{Fe}^{3+}$ on photocatalyst surface. For example, Fe^{3+} is more favourable to adsorb on WO_3 surface than Fe^{2+} (ref. 67).

Methods

Materials. SiO_2 and $\text{H}_2\text{PtCl}_6 \cdot 6\text{H}_2\text{O}$ were acquired from Aladdin, and the Na_3IrCl_6 was supplied from Alfa Aesar. Other reagents used in this work, including glucose, methanol, WO_3 , NaOH , $\text{CuSO}_4 \cdot 5\text{H}_2\text{O}$ and NaIO_3 were of analytical reagent grade and obtained from Sinopharm Chemical Reagent Co., Ltd. All of the above chemicals were used without further purification.

Preparation of Pt/SiC photocatalyst. The SiC nanoparticles were prepared by the carbothermic reduction method. Powders of SiO_2 and glucose were mixed in the molar ratio of $\text{Si:C} = 1:6$ and pulverized in a mortar to well disperse the mixed powders. The well-mixed powder was calcined under Ar atmosphere at 1450°C for 5 h at a rate of 2°C min^{-1} in a tubular furnace. The calcined powder was then cooled to room temperature and further purified to remove unreacted raw materials based on our previous report²⁶. Briefly, the sample was calcined under O_2 atmosphere at 873 K for 5 h and steeped with 10 wt% sodium hydroxide solution in order to remove free carbon and unreacted SiO_2 .

Platinum (Pt) was loaded on SiC by the photodeposition method as described in the following steps. The H_2PtCl_6 solution with a concentration of 1 mmol L^{-1} was mixed with SiC powder in a quartz cell. In the process of stirring, 2 mL of methanol was added into the mixture. After evacuation, the suspension was irradiated with a 125 W Hg lamp to load Pt nanoparticles onto the SiC. After a certain irradiation time, the obtained sample was washed thoroughly with deionized water and dried in vacuum for 1 h. The irradiation time was changed from 0.5 to 2 h to tune the content of Pt in sample, which was denoted as Pt-*x*h/SiC ($x = 0.5, 1, 1.5, 2$, representing the irradiation time).

Preparation of $\text{Cu}_2\text{O-Pt/SiC}$ and Pt/SiC/IrO_x photocatalysts. $\text{Cu}_2\text{O-Pt/SiC}$ and Pt/SiC/IrO_x photocatalysts were also prepared by the similar procedure by using Pt/SiC (Pt-1h/SiC) instead of pure SiC. In the preparation of $\text{Cu}_2\text{O-Pt/SiC}$, $\text{CuSO}_4 \cdot 5\text{H}_2\text{O}$ aqueous solution in the concentration of 0.6 mmol L^{-1} and 2 mL of methanol were introduced to the quartz cell together with Pt/SiC. The content of Cu species in the final sample was controlled by changing the irradiation time from 1 to 10 h, the resulting sample was denoted as $\text{Cu}_2\text{O-Pt-yh/SiC}$ ($y = 1, 3, 5, 8, 10$). For the synthesis of Pt/SiC/IrO_x , Na_3IrCl_6 and NaIO_3 aqueous solution with the respective concentration of 0.6 and 0.01 mol L^{-1} were added into the reactor to mix with Pt/SiC. The content of Ir species in the final sample was adjusted also by the irradiation time from 1 to 10 h, the resulting sample was denoted as $\text{Pt/SiC/IrO}_x-y\text{h}$ ($y = 1, 3, 5, 8, 10$). After IrO_x photodeposition, the samples were washed by deionized water and ethanol for several times to remove residual iodine species. The final sample was obtained after drying in vacuum for 1 h. In order to detect the residual iodine ions, the samples were immersed in the AgNO_3 solution. However, we did not find any precipitates AgIO_3 or AgI in solution, indicating iodine ion can be completely washed away in the synthesis process.

Preparation of $\text{Cu}_2\text{O-Pt/SiC/IrO}_x$ photocatalysts. Pt/SiC was added to the aqueous solution with $\text{CuSO}_4 \cdot 5\text{H}_2\text{O}$ (0.6 mmol L^{-1}) and Na_3IrCl_6 (0.6 mmol L^{-1})

followed by evacuation and irradiating with a 125 W Hg lamp. The content of Cu and Ir species in the final sample was controlled by the irradiation time from 3 to 15 h. The obtained sample was washed thoroughly with deionized water and dried in vacuum for 1 h, which was denoted as $\text{Cu}_2\text{O-Pt-zh/SiC/IrO}_x$ ($z = 3, 5, 8, 10, 12, 15$).

Preparation of Pt/WO_3 photocatalyst. Pt/WO_3 photocatalyst was also prepared by the photoreduction method similar to that in preparation of Pt/SiC photocatalyst with the irradiation time of 0.5 h.

Characterization of photocatalysts. XRD patterns were recorded with Ni filtered Cu K α radiation at 40 kV and 40 mA on a Bruker D8 Advance X-ray diffractometer. Morphology of sample was characterized by a field emission scanning electron microscopy (JSM-6700F) and TEM. TEM images were obtained at an accelerating voltage of 200 kV using a JEOL model JEM 2010 EX instrument. UV-Vis diffuse reflectance (UV-Vis DRS) spectra were obtained on a UV-Vis spectrophotometer (Cary 500) with a self-supporting sample cell, and the pure BaSO_4 was used as a reflectance standard. Brunauer-Emmett-Teller (BET) surface area was measured with an ASAP2020M apparatus (Micromeritics Instrument Corp., USA). Nitrogen adsorption and desorption isotherms were measured at 77 K. Contents of Pt, Cu and Ir in the samples were measured using an inductively coupled plasma optical emission spectrometer (Ultima 2, HORIBA Jobin Yvon Co., France). HS-LEIS measurements were carried out on an IonTOF Qtac100 low-energy ion scattering analyser. $^4\text{He}^+$ ions with a kinetic energy of 3 keV were applied at a low ion flux equal to 1325 pA cm^{-2} , which was necessary to avoid the sputtering of surfaces. $^{20}\text{Ne}^+$ ions with a kinetic energy of 5 keV were applied at a low ion flux equal to 445 pA cm^{-2} . The scattering angle was 145° . XPS measurements were performed on a Quantum 2000 Scanning ESCA Microprobe (Physical Electronics) using Al K α radiation (1846.6 eV) as the X-ray source. ^{13}C NMR spectra were recorded on AVANCE III 400 MHz spectrometer using TMS as the internal standard. $^{13}\text{CO}_2$ and H_2^{18}O were employed as the reactants in the isotope labelling comparison reaction instead of CO_2 and H_2O , respectively. After irradiation, the reaction solution was characterized with ^{13}C NMR directly. FT-IR experiments were carried out on a Nicolet 670 FT-IR spectrometer at a resolution of 4 cm^{-1} and 64 scans. FT-IR experiments were performed in a home-made IR cell in conjunction with a vacuum system. The catalyst powders were first pressed into a self-supporting disk (18 mm diameter, 20 mg), and then the disk was placed in the sample cell, which allowed the disk to move vertically along the cell tube. Prior to the FT-IR measurements, the disk was treated under a dynamic vacuum (10^{-4} Torr) at 473 K for 2 h. After cooling the disk to room temperature, CO_2 was introduced into the cell via the septum with a syringe. Photoluminescence excitation spectra was recorded on a FL/FS920 spectrofluorimeter (Edinburgh Instruments) fluorescence spectrometer at room temperature; the excitation wavelength is 375 nm.

CO_2 photoreduction apparatus and reactions. The spatially separated Z-scheme system includes a CO_2 -reduction chamber and an O_2 -generation chamber that are divided by a Nafion membrane (The circular Nafion membrane was Fe-ion exchanged before used in the reactor.) (Supplementary Fig. 6). The cubage of each reaction chamber is 300 mL. The aqueous solution containing 50 mg photocatalyst (SiC, Pt/SiC, $\text{Cu}_2\text{O-Pt/SiC}$, Pt/SiC/IrO_x or $\text{Cu}_2\text{O-Pt/SiC/IrO}_x$) and 2 mM FeCl_2 and another aqueous solution containing 100 mg Pt/WO_3 and 2 mM FeCl_3 were added to the two reaction chambers, respectively. The pH of solutions was adjusted to 2.3 by adding hydrochloric acid to prevent hydrolysis of the iron ions. Prior to irradiation, ultra-pure Ar (99.9995 v%) gas was bubbled through the solution to purge any dissolved air in the O_2 -generation compartment and filled to atmospheric pressure, while ultra-pure CO_2 gas was bubbled through the solution in the CO_2 -reduction chamber and filled to atmospheric pressure. During the photoreaction, the solution in each chamber was stirred and irradiated with a 300 W xenon (Xe) lamp. The lamp with an optical filter ($\lambda \geq 420 \text{ nm}$) was vertically placed at equal distance from each chamber, which makes both solutions to receive the same amount of visible light intensity. The solution in the CO_2 -reduction chamber was sampled every 2 h and analysed by ion chromatography (IC, Thermofisher ICS 1100) after filtering catalyst. The gaseous products in O_2 evolution chamber were sampled every 2 h by an off-line sampling syringe (0.5 mL) and then analysed by the gas chromatography (GC, Agilent 7890B, TCD detector) using ultra-pure Ar as the carrier gas.

Photoelectrochemical measurements. Photoelectrochemical measurements were carried out with a BAS Epsilon workstation using a standard three-electrode electrochemical cell with a working electrode, a platinum foil as the counter electrode, and a saturated Ag/AgCl electrode as the reference. A sodium sulfate solution (0.2 M) was used as the electrolyte, and a 300 W Xe lamp ($\lambda = 320\text{--}780 \text{ nm}$) as the light source. The working electrode was prepared by FTO glass pieces, which was cleaned by sonication in cleanout fluid, acetone and ethanol in sequence prior to use. The photocatalyst was dispersed in ethanol under sonication to form a suspension. A photocatalyst film was fabricated by spreading the suspension onto the conductive surface of the FTO glass.

Data availability

The data that support the findings of this study are available from the corresponding author upon reasonable request. [Source data](#) are provided with this paper.

Received: 25 November 2019; Accepted: 13 May 2020;

Published online: 16 June 2020

References

- Rao, H., Schmidt, L. C., Bonin, J. & Robert, M. Visible-light-driven methane formation from CO₂ with a molecular iron catalyst. *Nature* **548**, 74–77 (2017).
- Voiry, D., Shin, H. S., Loh, K. P. & Chhowalla, M. Low-dimensional catalysts for hydrogen evolution and CO₂ reduction. *Nat. Rev. Chem.* **2**, 17105 (2018).
- Yu, J., Low, J., Xiao, W., Zhou, P. & Jaroniec, M. Enhanced photocatalytic CO₂-reduction activity of anatase TiO₂ by coexposed {001} and {101} facets. *J. Am. Chem. Soc.* **136**, 8839–8842 (2014).
- Wang, S., Guan, B. Y. & Lou, X. W. Rationally designed hierarchical N-doped carbon@NiCo₂O₄ double-shelled nanoboxes for enhanced visible light CO₂ reduction. *Energy Environ. Sci.* **11**, 306–310 (2018).
- Ran, J., Jaroniec, M. & Qiao, S. Z. Cocatalysts in semiconductor-based photocatalytic CO₂ reduction: achievements, challenges, and opportunities. *Adv. Mater.* **30**, 1704649 (2018).
- Sun, Z. et al. Catalysis of carbon dioxide photoreduction on nanosheets: fundamentals and challenges. *Angew. Chem. Int. Ed.* **57**, 7610–7627 (2018).
- Dong, C. et al. Size-dependent activity and selectivity of carbon dioxide photocatalytic reduction over platinum nanoparticles. *Nat. Commun.* **9**, 1252 (2018).
- Leitner, W. Carbon dioxide as a raw material: the synthesis of formic acid and its derivatives from CO₂. *Angew. Chem. Int. Ed.* **34**, 2207–2221 (1995).
- Mura, M. G., Luca, L. D., Giacomelli, G. & Porcheddu, A. Formic acid: a promising bio-renewable feedstock for fine chemicals. *Adv. Synth. Catal.* **354**, 3180–3186 (2012).
- Sekizawa, K., Maeda, K., Domen, K., Koike, K. & Ishitani, O. Artificial Z-scheme constructed with a supramolecular metal complex and semiconductor for the photocatalytic reduction of CO₂. *J. Am. Chem. Soc.* **135**, 4596–4599 (2013).
- Li, L. et al. Effective visible-light driven CO₂ photoreduction via a promising bifunctional iridium coordination polymer. *Chem. Sci.* **5**, 3808–3813 (2014).
- Liu, X., Inagaki, S. & Gong, J. Heterogeneous molecular systems for photocatalytic CO₂ reduction with water oxidation. *Angew. Chem. Int. Ed.* **55**, 14924–14950 (2016).
- Wang, W. H., Himeda, Y., Muckerman, J. T., Manbeck, G. F. & Fujita, E. CO₂ hydrogenation to formate and methanol as an alternative to photo- and electrochemical CO₂ reduction. *Chem. Rev.* **115**, 12936–12973 (2015).
- Habisreutinger, S. N., Schmidt-Mende, L. & Stolarczyk, J. K. Photocatalytic reduction of CO₂ on TiO₂ and other semiconductors. *Angew. Chem. Int. Ed.* **52**, 7372–7408 (2013).
- Xu, Y. F. et al. A CsPbBr₃ perovskite quantum dot/graphene oxide composite for photocatalytic CO₂ reduction. *J. Am. Chem. Soc.* **139**, 5660–5663 (2017).
- Sheng, H. et al. Carbon dioxide dimer radical anion as surface intermediate of photoinduced CO₂ reduction at aqueous Cu and CdSe nanoparticle catalysts by rapid-scan FT-IR spectroscopy. *J. Am. Chem. Soc.* **140**, 4363–4371 (2018).
- Fu, Y. et al. An amine-functionalized titanium metal-organic framework photocatalyst with visible-light-induced activity for CO₂ reduction. *Angew. Chem. Int. Ed.* **51**, 3420–3423 (2012).
- Wang, D., Huang, R., Liu, W., Sun, D. & Li, Z. Fe-based MOFs for photocatalytic CO₂ reduction: role of coordination unsaturated sites and dual excitation pathways. *ACS Catal.* **4**, 4254–4260 (2014).
- Kuriki, R. et al. Nature-inspired, highly durable CO₂ reduction system consisting of a binuclear Ruthenium(II) complex and an organic semiconductor using visible light. *J. Am. Chem. Soc.* **138**, 5159–5170 (2016).
- Kuriki, R. et al. Robust binding between carbon nitride nanosheets and a binuclear Ruthenium(II) complex enabling durable, selective CO₂ reduction under visible light in aqueous solution. *Angew. Chem. Int. Ed.* **56**, 4867–4871 (2017).
- Takeda, H. et al. Highly efficient and robust photocatalytic systems for CO₂ reduction consisting of a Cu(I) photosensitizer and Mn(II) catalysts. *J. Am. Chem. Soc.* **140**, 17241–17254 (2018).
- Zhou, B. et al. Mo–Bi–Cd ternary metal chalcogenides: highly efficient photocatalyst for CO₂ reduction to formic acid under visible light. *ACS Sustain. Chem. Eng.* **6**, 5754–5759 (2018).
- Jia, L., Li, J. & Fang, W. Enhanced visible-light active C and Fe co-doped LaCoO₃ for reduction of carbon dioxide. *Catal. Commun.* **11**, 87–90 (2009).
- Stolarczyk, J. K., Bhattacharyya, S., Polavarapu, L. & Feldmann, J. Challenges and prospects in solar water splitting and CO₂ reduction with inorganic and hybrid nanostructures. *ACS Catal.* **8**, 3602–3635 (2018).
- Guo, X. et al. High photoelectrocatalytic performance of a MoS₂–SiC hybrid structure for hydrogen evolution reaction. *J. Mater. Chem. A* **1**, 4657–4661 (2013).
- Wang, Y. et al. Visible-light driven overall conversion of CO₂ and H₂O to CH₄ and O₂ on 3D-SiC@2D-MoS₂ heterostructure. *J. Am. Chem. Soc.* **140**, 14595–14598 (2018).
- Inoue, T., Fujishima, A., Konishi, S. & Honda, K. Photoelectrocatalytic reduction of carbon dioxide in aqueous suspensions of semiconductor powders. *Nature* **277**, 637–638 (1979).
- Mnatsakanov, T. T., Levinshstein, M. E., Pomortseva, L. I. & Yurkov, S. N. Carrier mobility model for simulation of SiC-based electronic devices. *Semicond. Sci. Technol.* **17**, 974–977 (2002).
- Nishino, S., Powell, J. A. & Will, H. A. Production of large-area single-crystal wafers of cubic SiC for semiconductor devices. *Appl. Phys. Lett.* **42**, 460–462 (1983).
- Gao, P., Liu, J., Lee, S., Zhang, T. & Sun, D. D. High quality graphene oxide-CdS-Pt nanocomposites for efficient photocatalytic hydrogen evolution. *J. Mater. Chem.* **22**, 2292–2298 (2012).
- Kim, Y. K. & Park, H. Light-harvesting multi-walled carbon nanotubes and CdS hybrids: application to photocatalytic hydrogen production from water. *Energy Environ. Sci.* **4**, 685–694 (2014).
- Zhai, Q. et al. Photocatalytic conversion of carbon dioxide with water into methane: platinum and copper(I) oxide co-catalysts with a core-shell structure. *Angew. Chem. Int. Ed.* **52**, 5776–5779 (2013).
- Wang, L. et al. Silica direct evaporation: a size-controlled approach to SiC/carbon nanosheet composites as Pt catalyst supports for superior methanol electrooxidation. *J. Mater. Chem. A* **3**, 24139–24147 (2015).
- Li, Q. et al. High-activity PtRuPd/C catalyst for direct dimethyl ether fuel cells. *Angew. Chem. Int. Ed.* **54**, 7524–7528 (2015).
- Zhou, Z. et al. Cultivating crystal lattice distortion in IrO₂ via coupling with MnO₂ to boost the oxygen evolution reaction with high intrinsic activity. *Chem. Commun.* **54**, 4959–4962 (2018).
- Hatanaka, M. et al. Reversible changes in the Pt oxidation state and nanostructure on a ceria-based supported Pt. *J. Catal.* **266**, 182–190 (2009).
- Wu, S. C., Tan, C. S. & Huang, M. H. Strong facet effects on interfacial charge transfer revealed through the examination of photocatalytic activities of various Cu₂O–ZnO heterostructures. *Adv. Funct. Mater.* **27**, 1604635 (2017).
- Lettenmeier, P. et al. Nanosized IrOx–Ir catalyst with relevant activity for anodes of proton exchange membrane electrolysis produced by a cost-effective procedure. *Angew. Chem. Int. Ed.* **55**, 742–746 (2016).
- Moulder, J., Stickle, W. F., Sobol, P. E., Bomben, K. D. & Chastain, J. *Handbook of X-Ray Photoelectron Spectroscopy: A Reference Book of Standard Spectra for Identification and Interpretation of XPS Data* (Perkin Elmer Corporation, 1992).
- Hatanaka, M. et al. Reversible changes in the Pt oxidation state and nanostructure on a ceria-based supported Pt. *J. Catal.* **266**, 182–190 (2009).
- Ye, W. et al. Enhanced O₂ reduction on atomically thin Pt-based nanoshells by integrating surface facet, interfacial electronic, and substrate stabilization effects. *Nano Res.* **11**, 3313 (2018).
- Lee, W. H., Liao, C. H., Tsai, M. F., Huang, C. W. & Wu, J. C. S. A novel twin reactor for CO₂ photoreduction to mimic artificial photosynthesis. *Appl. Catal. B Environ.* **132–133**, 445–451 (2013).
- Yu, S. C. et al. A novel membrane reactor for separating hydrogen and oxygen in photocatalytic water splitting. *J. Membr. Sci.* **382**, 291–299 (2011).
- Cho, S.-H. et al. Synergistic coupling of metallic cobalt nitride nanofibers and IrO_x nanoparticle catalysts for stable oxygen evolution. *Chem. Mater.* **30**, 5941–5950 (2018).
- Kwon, T. et al. Cobalt assisted synthesis of IrCu hollow octahedral nanocages as highly active electrocatalysts toward oxygen evolution reaction. *Adv. Funct. Mater.* **27**, 1604688 (2017).
- Pfeifer, V. et al. The electronic structure of iridium oxide electrodes active in water splitting. *Phys. Chem. Chem. Phys.* **18**, 2292–2296 (2016).
- Li, P., Kong, L., Liu, J., Yan, J. & Liu, S. Photoassisted hydrothermal synthesis of IrO_x–TiO₂ for enhanced water oxidation. *ACS Sustain. Chem. Eng.* **7**, 17941–17949 (2019).
- Esquiús, J. R. et al. Effect of base on the facile hydrothermal preparation of highly active IrOx oxygen evolution catalysts. *ACS Appl. Energy Mater.* **3**, 800–809 (2020).
- Cheng, H. et al. Aging amorphous/crystalline heterophase PdCu nanosheets for catalytic reactions. *Natl. Sci. Rev.* **6**, 955–961 (2019).
- Frame, F. A. et al. Photocatalytic water oxidation with nonsensitized IrO₂ nanocrystals under visible and UV light. *J. Am. Chem. Soc.* **133**, 7264–7267 (2011).
- Nakada, A., Koike, K., Nakashima, T., Morimoto, T. & Ishitani, O. Photocatalytic CO₂ reduction to formic acid using a Ru(II)–Re(I) supramolecular complex in an aqueous solution. *Inorg. Chem.* **54**, 1800–1807 (2015).
- Zeng, Z. et al. Boosting the photocatalytic ability of Cu₂O nanowires for CO₂ conversion by MXene quantum dots. *Adv. Funct. Mater.* **29**, 1806500 (2019).

53. Bhattacharyya, K. et al. Role of the surface lewis acid and base sites in the adsorption of CO₂ on titania nanotubes and platinumized titania nanotubes: an in situ FT-IR study. *J. Phys. Chem. C* **117**, 12661–12678 (2013).
54. Vayssilov, G. N., Mihaylov, M., Petkov, P. S., Hadjiivanov, K. I. & Neyman, K. M. Reassignment of the vibrational spectra of carbonates, formates, and related surface species on Ceria: a combined density functional and infrared spectroscopy investigation. *J. Phys. Chem. C* **115**, 23435–23454 (2011).
55. Kaneco, S., Kurimoto, H., Shimizu, Y., Ohta, K. & Mizuno, T. Photocatalytic reduction of CO₂ using TiO₂ powders in supercritical fluid CO₂. *Energy* **24**, 21–30 (1999).
56. Tamaki, Y., Koike, K. & Ishitani, O. Highly efficient, selective, and durable photocatalytic system for CO₂ reduction to formic acid. *Chem. Sci.* **6**, 7213–7221 (2015).
57. Xu, S. J., Yu, M. B., Rusli, U., Yoon, S. F. & Che, C. M. Time-resolved photoluminescence spectra of strong visible light-emitting SiC nanocrystalline films on Si deposited by electron-cyclotron-resonance chemical-vapor deposition. *Appl. Phys. Lett.* **76**, 2550–2552 (2000).
58. Liang, L. et al. Single unit cell bismuth tungstate layers realizing robust solar CO₂ reduction to methanol. *Angew. Chem. Int. Ed.* **54**, 13971–13974 (2015).
59. Dozzi, M. V., D'Andrea, C., Ohtani, B., Valentini, G. & Selli, E. Fluorine-doped TiO₂ materials: photocatalytic activity vs time-resolved photoluminescence. *J. Phys. Chem. C* **117**, 25586–25595 (2013).
60. Islam, M. J. et al. An oxygen-vacancy rich 3D novel hierarchical MoS₂/BiOI/AgI ternary nanocomposite: enhanced photocatalytic activity through photogenerated electron shuttling in a Z-scheme manner. *Phys. Chem. Chem. Phys.* **18**, 24984–24993 (2016).
61. Kim, C., Cho, K. M., Al-Saggaf, A., Gereige, I. & Jung, H. T. Z-scheme photocatalytic CO₂ conversion on three-dimensional BiVO₄/carbon-coated Cu₂O nanowire arrays under visible light. *ACS Catal.* **8**, 4170–4177 (2018).
62. Pu, Y. C., Lin, W. H. & Hsu, Y. J. Modulation of charge carrier dynamics of Na_xH_{2-x}Ti₃O₇-Au-Cu₂O Z-scheme nanoheterostructures through size effect. *Appl. Catal. B Environ.* **163**, 343–351 (2015).
63. Bae, K. L., Kim, J., Lim, C. K., Nam, K. M. & Song, H. Colloidal zinc oxide-copper(I) oxide nanocatalysts for selective aqueous photocatalytic carbon dioxide conversion into methane. *Nat. Commun.* **8**, 1156 (2017).
64. Meekins, B. H. & Kamat, P. V. Role of water oxidation catalyst IrO₂ in shuttling photogenerated holes across TiO₂ interface. *J. Phys. Chem. Lett.* **2**, 2304–2310 (2011).
65. Ma, Y. et al. Synergetic effect of dual cocatalysts in photocatalytic H₂ production on Pd-IrO_x/TiO₂: a new insight into dual cocatalyst location. *Phys. Chem. Chem. Phys.* **16**, 17734–17742 (2014).
66. Lo, C. C., Huang, C. W., Liao, C. H. & Wu, J. C. Novel twin reactor for separate evolution of hydrogen and oxygen in photocatalytic water splitting. *Int. J. Hydrog. Energ.* **35**, 1523–1529 (2010).
67. Tomita, O. et al. Improved photocatalytic water oxidation with Fe₃⁺/Fe₂⁺ redox on rectangular-shaped WO₃ particles with specifically exposed crystal faces via hydrothermal synthesis. *Chem. Lett.* **46**, 221–224 (2017).

Acknowledgements

The work is financially supported by the National Natural Science Foundation of China (grants no. 21673042, 51702053, 21673043, 21972020).

Author contributions

Y.W., Z.Z. and X.W. conceived the research. Y.W. and X.S. prepared photocatalysts and conducted all the experiments. J.L. performed the electrochemistry measurement. J.S. offered help to analyse the characterization experiment data. Y.W., Z.Z., X.W. and C.L. wrote and revised the manuscript. D.W., J.C.S.W. and X.F. gave suggestions on the experiment and writing.

Competing interests

The authors declare no competing interests.

Additional information

Supplementary information is available for this paper at <https://doi.org/10.1038/s41467-020-16742-3>.

Correspondence and requests for materials should be addressed to Z.Z., J.C.S.W., X.W. or C.L.

Peer review information *Nature Communications* thanks Bien Tan, Mingyang Xing and the other, anonymous, reviewer(s) for their contribution to the peer review of this work. Peer reviewer reports are available.

Reprints and permission information is available at <http://www.nature.com/reprints>

Publisher's note Springer Nature remains neutral with regard to jurisdictional claims in published maps and institutional affiliations.



Open Access This article is licensed under a Creative Commons

Attribution 4.0 International License, which permits use, sharing, adaptation, distribution and reproduction in any medium or format, as long as you give appropriate credit to the original author(s) and the source, provide a link to the Creative Commons license, and indicate if changes were made. The images or other third party material in this article are included in the article's Creative Commons license, unless indicated otherwise in a credit line to the material. If material is not included in the article's Creative Commons license and your intended use is not permitted by statutory regulation or exceeds the permitted use, you will need to obtain permission directly from the copyright holder. To view a copy of this license, visit <http://creativecommons.org/licenses/by/4.0/>.

© The Author(s) 2020